Applied Radiation and Isotopes 226 (2025) 112243

Contents lists available at ScienceDirect

Applied Radiation and Isotopes

journal homepage: www.elsevier.com/locate/apradiso

$^{134/137}$Cs isotopes discrimination via a β/γ time-coincidence energy gating digital autoradiographic system

S. Duval [a,*], M. Libes De Geyter [a], A. Bongrand [b], E. Morteau [c], M. Siitari-Kauppi [d], J.W.L. Ang [e]

[a] AI4R S.A.S., 2 rue Alfred Kastler, 44300, Nantes, France
[b] Nantes Angers Cancer and Immunology Research Center, 8 quai Moncousu, 44000, Nantes, France
[c] Subatech, UMR 6457, 2 rue Alfred Kastler, 44300, Nantes, France
[d] University of Helsinki, Chemistry Department, Helsinki, Finland
[e] Singapore Nuclear Research and Safety Institute, Singapore, Singapore

ARTICLE INFO

Keywords:
β/γ coincidence imaging
Digital autoradiography
Counting mode imaging
Gamma spectroscopy
Gaseous detector
SiPM

ABSTRACT

Since the discovery of radioactivity, autoradiography has been extensively used in nuclear physics to characterize the distribution of radionuclides into biological or inert samples. In this study, we present an original add-on method to the real-time digital autoradiography, aiming at identifying ^{134}Cs from ^{137}Cs events in radioactive maps measured from sample surface on the basis of a micro-pattern gaseous detector coupled to a crystal-based photon scintillation detector. Using the fast timing of both instruments, we successfully demonstrated the possibility of discriminating both isotopes and quantifying their isotopic ratios. In particular, we achieved a rejection rate of ^{137}Cs events close to 100 % while maintaining high-resolution mapping of ^{134}Cs distributions. Tests mixed samples showed strong linear correlations between detected event ratios and known isotope activities. This emerging method offers a promising tool for radiocesium source attribution and further opens new perspectives in digital autoradiography for multi-isotope mapping in complex materials.

1. Introduction

A persistent challenge in the field of autoradiography is the discrimination of isotopes with nearly identical beta energy spectra. Previous work by Ang et al. (2023) attempted to separate the individual contributions of ^{134}Cs and ^{137}Cs in mixtures by analyzing the intensity of charge signals measured by the gas proportional detector anode. However, the very similar electron energies produced by these isotopes hinder effective discrimination when relying solely on beta spectrometry. The cesium isotopic pair has been studied extensively due to its relevance in environmental contamination scenarios (Wai et al., 2020). Originating from nuclear industry or weapon tests, involving ^{235}U or other isotopes fission, these two isotopes can be transported over great distances by solubilization in water, aerosol trapping in air and concentrate into sparingly-soluble particulate form (Ikehara et al., 2020). These characteristics, combined with their relatively long half-life, make them a source of radiation dose (Ang et al., 2024). As outlined in studies (Ang et al., 2023), (Chino et al., 2016), the ratio of ^{134}Cs to ^{137}Cs can provide crucial insights into the origin and evolution of radiocesium in contaminated areas.

Digital autoradiography is a 2D imaging technique that quantitatively determines the distribution of radioisotopes from the sample surface at a micrometric scale (Bäck and Jacobsson, 2010), (Miller et al., 2014). Recent advancements in digital autoradiography have expanded its capabilities beyond spatial mapping; real-time counting records individual event position, time, and energy into a file list-mode format. For instance, spectroscopic autoradiography (Lefeuvre et al., 2024), (Yamamoto et al., 2025) now provides energy-resolved data, while spatio-temporal approach (Sardini et al., 2024), (Donnard et al., 2025) enables the dynamic tracking of radioactive decay events and thus the characterization of radioelement decay chain parts. These latest developments offer complementary nuclear information alongside spatial data.

Autoradiography has been widely used to investigate radionuclide contaminants under decommissioning (Leskinen et al., 2013) and study the diffusion properties of radionuclides in granitic rock (Muuri et al., 2019), (Fabritius et al., 2024) in the context of final disposal of spent nuclear fuel and clay in the context of uranium mining site contamination studies (Billon et al., 2020). It has been concluded in previous sorption and diffusion studies that the rock heterogeneity may have a

* Corresponding author.
E-mail address: samuel.duval@ai4r.com (S. Duval).

https://doi.org/10.1016/j.apradiso.2025.112243
Received 7 August 2025; Received in revised form 2 October 2025; Accepted 5 October 2025
Available online 9 October 2025

significant effect on the transport properties of radionuclides in granitic rock, and the real-time digital autoradiography was found to be a practical tool for quantitatively assessing the heterogeneous diffusion and sorption of radionuclides in hard materials. The new technique presented in this article makes it possible to locate several radionuclides present in the same sample.

Methods have been developed to separate the contribution of β emitters in autoradiographic images. For example, separating ^{3}H from ^{14}C emissions (Donnard et al., 2009) relying on two different β emission mean energy spectra being 5.7 keV and 49.5 keV respectively (Livechart). Another discrimination strategy is based on the half-life difference of two radioelements (Barthe et al., 2004). More recently, a work of Adler et al. (2025) presented a novel coincidence setup combining a Timepix3 silicon detector and a scintillation crystal aiming at discriminating between alpha particles and positrons.

By combining spatially resolved autoradiography with nuclear time coincidence spectroscopic data, our method aims to extract detailed maps of radioisotope distributions. This integrated approach not only overcomes the limitations of beta spectrometry when distinguishing isotopes with similar electron energies but also paves the way for improved quantification and analysis of radioactive contaminants in environmental samples.

In this article, a novel β/γ time coincidence spectroscopic digital autoradiographic system specifically designed for the discrimination of $^{134}Cs/^{137}Cs$ radioisotopes is introduced. By simultaneously detecting β particles and the associated gamma and X-ray emissions, particularly the γ-rays from the decay of the ^{134}Cs, our approach leverages the unique nuclear signatures of each isotope. This approach offers possible solutions to the issues raised in the article (Ang et al., 2023). Hence, the β/γ time coincidence setup enhances the separation of ^{134}Cs and ^{137}Cs and improves the overall quantitative analysis of radiocesium in environmental and nuclear forensic applications.

2. Experimental setup and data acquisition

The experimental prototype consists of two major components (see Fig. 1a and b), the NaI(Tl) scintillator coupled to a silicon photomultiplier (SiPM 51B51/SIP-E3-X from SCIONIX™) that was mounted on top of a custom-made parallel ionization multiplier micro-pattern gaseous detector (PIM-MPGD (Donnard et al., 2009)) based on the commercially available BeaQuant-S real-time digital autoradiograph. Fig. 1 c illustrates the block diagram of the hybrid device showing a β/γ coincidence event. The β interacts into the gas sensitive volume of the PIM-MPGD while the γ photon deposes its energy into the scintillating crystal.

2.1. Real-time digital autoradiography with the PIM-MPGD device (x_β, y_β)

The core of the autoradiograph system is its micro-pattern gaseous detector (Fig. 2 a), which is dedicated to the direct detection of charged particles-specifically β emissions from radioactive samples. In this configuration, the anode plays a crucial role in reading and processing the induced signals generated by these particles. When a radioactive decay occurs, beta particles traverse the gas-filled chamber of the detector. Along their paths, they ionize the gas molecules, creating electron–ion pairs. Under the influence of an applied electric field, the liberated electrons drift toward the amplification region near the anode. In this region, the electrons undergo avalanche multiplication, producing a localized cloud of charges that significantly amplifies the original ionization signal. These amplified charges generate an induced signal on the multi-layer anode circuit board which is designed with a finely segmented chess board readout structure (square readout pads of 300 μm with a 400 μm pitch (Fig. 2 b) to ensure high spatial resolution reconstructed images. A similar structure is depicted in (Donnard et al., 2009) for detailed explanation. The anode configuration and associated electronics allow it to register the exact position of each decay event (counting mode) with spatial resolutions reaching about 25 to 35 μm for standard β and α particles respectively ((Ang et al., 2024), (Donnard et al., 2009)). Such precision is essential for constructing detailed two-dimensional autoradiographs of the sample at the microscopic scale. The signals acquired by the anode are simultaneously digitized using a multichannel readout system triggered by the signal induced on the Frisch grid readout electrode (Fig. 2 a).

In the setup, seven of the eight 64-channels cards are dedicated to processing these position relative signals from the anode with three cards dedicated to the X position and four cards to the Y position, covering collectively a field of view of 102.4 mm × 76.8 mm. The collected data are subsequently processed through the dedicated acquisition software Beavacq, enabling the reconstruction of raw data *.acq files converted into *.root files. These can be processed with CERN ROOT framework and libraries (version 6.34), allowing the reconstruction of high-resolution images that accurately map the spatial distribution of reconstructed positions of radioactive decays (x_β, y_β) within the sample.

Fig. 3 illustrates a typical signal registered on the Y-cards along the y-axis, with the four shades of blue representing the four individual cards. In this example, the charge signal is distributed across 5 channels, as shown by the magnified view. To determine the y_β position, a Gaussian fit is applied to the signal, yielding a value of 141.44 mm in this case. The same methodology is employed to determine the x_β coordinate.

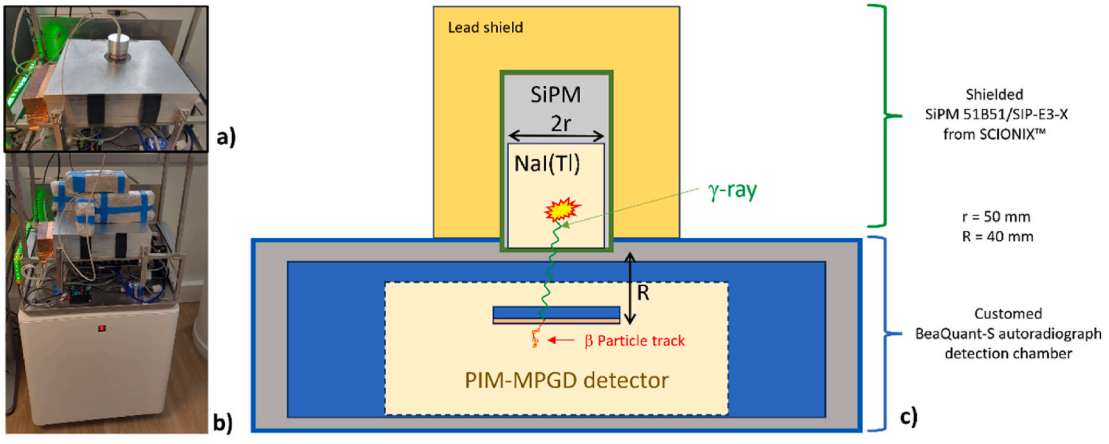

Fig. 1. a) Photographs of the NaI/SiPM scintillator and b) of the BeaQuant-S autoradiograph. c) Block diagram of the β/γ coincidence device.

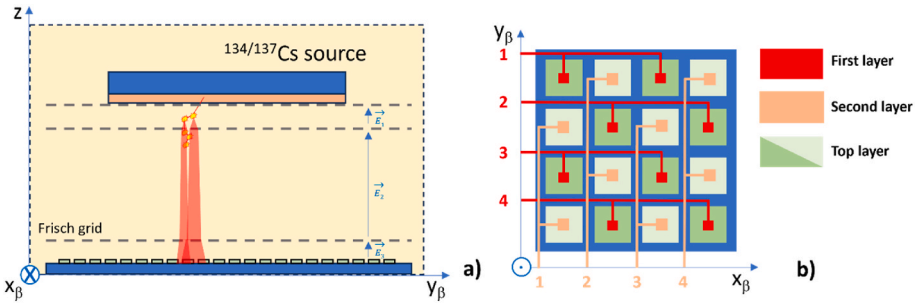

Fig. 2. a) Schematic diagram showing a cross section through the gas detection chamber showing an example of an emitted β particle, its multiple interactions and the amplification avalanche. b) Zoom on 4x4 readout pads of the anode multi-layer structure. Each layer of the printed circuit board is illustrated with a specific color. (For interpretation of the references to color in this figure legend, the reader is referred to the Web version of this article.)

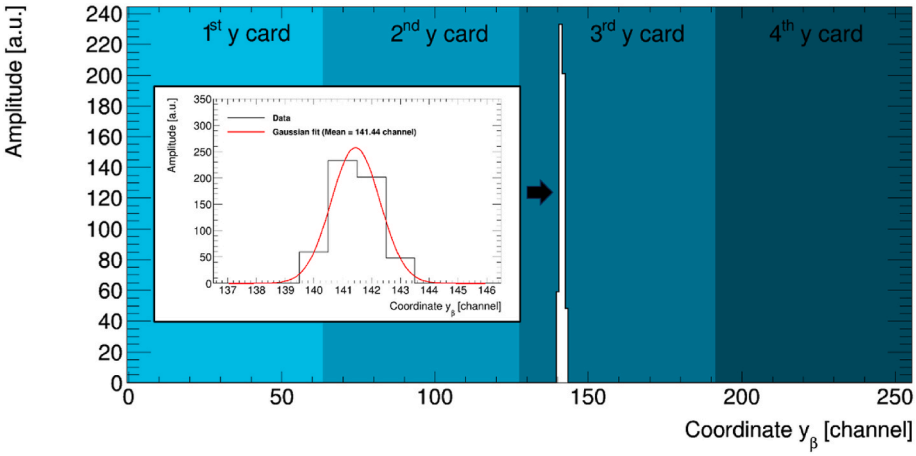

Fig. 3. β induced signal on Y-Position-related channels of the detector. Colors index the four 64-bin cards. (For interpretation of the references to color in this figure legend, the reader is referred to the Web version of this article.)

2.2. A one channel gamma spectroscopic system: NaI(Tl)/SiPM (E_γ)

The scintillation detection system used in this study employs a NaI (Tl) crystal coupled with a Silicon Photomultiplier (SiPM) for gamma-ray detection. The SiPM is an array of avalanche photodiodes operating in Geiger mode, providing high sensitivity and fast timing capabilities with a pulse rise time of 560 ns in this specific configuration. This configuration was chosen for its compact design, low operating voltage (5 V), an energy resolution measured at 7 % (FWHM) @ 796 keV (see Fig. 8) and affordable price, making it an ideal candidate to integrate gamma spectroscopy into the autoradiographic system and deliver a proof of concept. The scintillation pulses are processed to extract energy and timing information.

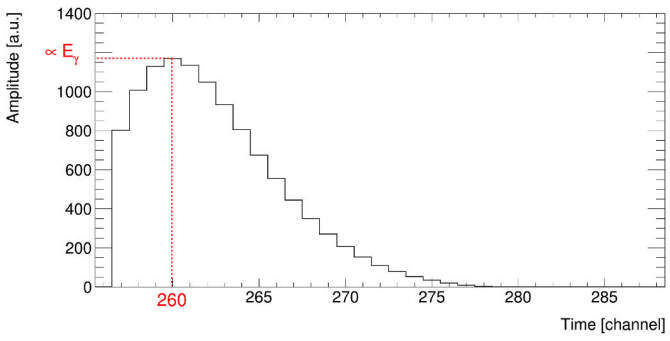

Fig. 4. A typical gamma signal sampled at 2.5 MHz on the energy-related channels.

Fig. 4 illustrates the digitized pulse amplitude of NaI(Tl)/SiPM for a single event, sampled over 32 time-related channels at a rate of 2.5 MHz. Consequently, each time sample has a duration of 400 ns. The pulse amplitude values are directly proportional to the energy deposited by the gamma-ray photon in the scintillator, denoted as E_γ. To establish a relationship between the arbitrary units provided by the scintillator and the energy in keV, a calibration was performed by measuring the three γ-ray lines from ^{134}Cs and ^{137}Cs spectrum.

2.3. $A^{134}Cs/^{137}Cs$ coincidence imaging system for (x_β, y_β, E_γ) triplet determination

The β/γ time coincidence system principle depicted in this article is based on a specific experimental setup which aims to capture only the photon signal at the instant a β particle triggers the autoradiograph electronics. When an electron cloud crosses the anode Frisch grid the NaI scintillator signals is recorded providing its time-related signal on the data acquisition card. To identify coincident photon emission with β decay, a time window of 1.2 μs is applied. The scintillation signal amplitude, corresponding to the highest channel value, is associated with the coordinates x_β, y_β, forming the triplet (x_β, y_β, E_γ).

2.4. ^{134}Cs and ^{137}Cs samples

2.4.1. Characteristics of 134/137 isotopes of cesium

The two decay schemes illustrated in Fig. 5 depict the decay processes and corresponding γ emissions of ^{134}Cs and ^{137}Cs.

In the ^{134}Cs decay scheme, one can observe two gamma emissions (underlined in red) with energies of 796 keV and 605 keV and global

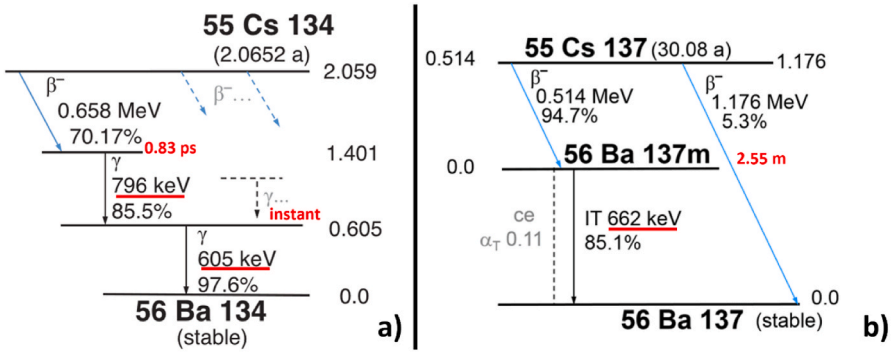

Fig. 5. a) Simplified decay scheme of ^{134}Cs and b) of ^{137}Cs (Soti et al., 2019).

occurrence probabilities of 59.9 % and 58.5 % respectively. Furthermore, these emissions are almost instantaneous as the excited states have a short lifetime less than a picosecond. Conversely, the decay of ^{137}Cs is characterized by only delayed gamma rays. Indeed, the daughter nucleus, ^{137m}Ba, emits gamma rays with a reported lifetime of 2.55 min. This delayed gamma emission minimizes the probability of coincidental detection, thereby allowing us to discriminate ^{137}Cs events more reliably. Lastly, the most probable X-rays originated from the ^{137}Cs are presented in Table 1.

To specifically identify events associated with ^{134}Cs, we have chosen to take advantage of the gamma information that is emitted concurrently with beta particles.

2.4.2. Pure samples of ^{134}Cs and ^{137}Cs

In order to demonstrate the capability of the discrimination method, we used a pure ^{134}Cs-radiolabelled particulate sample (total activity of 173 Bq) and pure ^{137}Cs thin layer sample (total activity of 131.5 Bq). Both samples were synthesized from our previous work (more details can be found in (Ang et al., 2023)).

For the thin layer sample, 10 µL of ^{137}Cs solution was deposited onto a petrographic glass slide, evaporated, and packaged in an ultra-thin Mylar® film (3 µm thick, see Fig. 6 a) to prevent any radiochemical contamination of the detector electrode resulting in an approximately 4.5 Bq/mm^2 surface activity.

For the particulate sample, copper hexacyanoferrate (Cu-HCF) microparticles were labeled with ^{134}Cs, mixed with non-radioactive quartz, and embedded in Araldite® resin on a petrographic glass slide (Fig. 6 b). The sample was polished to 70 ± 40 µm thickness.

Both samples were placed side by side on the same sample holder, with sample side facing the PIM-MPGD, in contact with the first micromesh, and measured continuously for 23 h.

2.4.3. Mixtures of ^{134}Cs/^{137}Cs

To quantify the linearity of the separation method, thin layer mixed samples of ^{134}Cs/^{137}Cs (same preparation as the ^{137}Cs sample in Fig. 6 a) with different isotopic ratios and two pure ^{137}Cs and ^{134}Cs ones were imaged during 3 h, and the separation algorithm was subsequently applied to determine the fraction of events attributable solely to ^{134}Cs among all events present in the autoradiographic image.

The five different ratios, pinpointed by A_{Ri} with i being an integer from 0 to 4, represent different ratios of ^{134}Cs activity to the total activity of the two isotopes (detailed in Table 2).

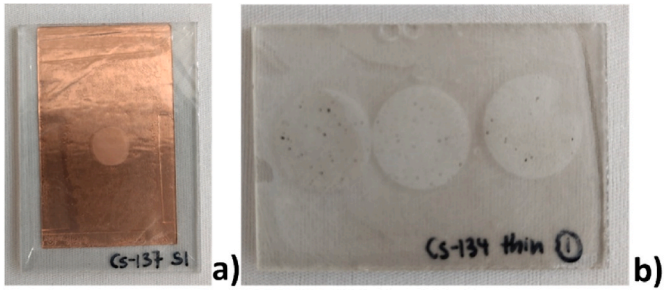

Fig. 6. a) Photographs of the ^{137}Cs and b) ^{134}Cs samples.

3. Results

3.1. Discrimination of pure samples (^{134}Cs) and (^{137}Cs)

3.1.1. Total gamma spectrum

Fig. 7 displays the total γ particle energy spectrum acquired with the SiPM of the two pure ^{134}Cs and ^{137}Cs samples over 23 h. Each scintillation signal above a threshold has been digitized and the amplitude used to construct the energy distribution. It was observed that the gamma peaks at 605 keV (attributed to ^{134}Cs) and 662 keV (attributed to ^{137}Cs) were insufficiently resolved to be differentiated. In contrast, the 796 keV gamma peak, which originates from ^{134}Cs, was clearly separated from the overlapping signals. Consequently, energy discrimination between the ^{134}Cs and ^{137}Cs sources would be achieved by applying an energy window centered around the 796 keV signal. A peak around 1400 keV is noticeable. It is linked to the sum of the two gammas of the ^{134}Cs which in some cases appear due to true coincidence summing and a contribution of the ^{40}K gamma at 1461 keV.

3.1.2. Gamma spectrum with β/γ coincidence

A more refined approach to gamma detection involves triggering the scintillator input only when a beta particle is detected by the PIM-MPGD device. Ideally, the photon input signal would only be recorded in time

Table 1
Most probable X-rays of ^{137}Cs ("Livechart).

Energy [keV]	Intensity (abs) [%]	Line
3.956–5.975	0.91 (4)	L
31.816	1.99 (3)	K-L_2
32.193	3.67 (6)	K-L_3
36.304–36.660	1.079 (20)	K-$M_{2,3,4}$
36.304–37.350	1.35 (2)	K-MN

Table 2
Characteristics of ^{134}Cs/^{137}Cs samples mixtures. Activity reported were decay corrected to the date of measurement with the β/γ coincidence device.

Samples	A_{R0}	A_{R1}	A_{R2}	A_{R3}	A_{R4}
^{134}Cs activity (Bq)	–	2.2	6.7	7.1	28.9
^{137}Cs activity (Bq)	131.5	31.5	30.3	9.5	–
Activity ratio (^{134}Cs to total activity)	0 %	6.5 %	18.1 %	42.8 %	100 %

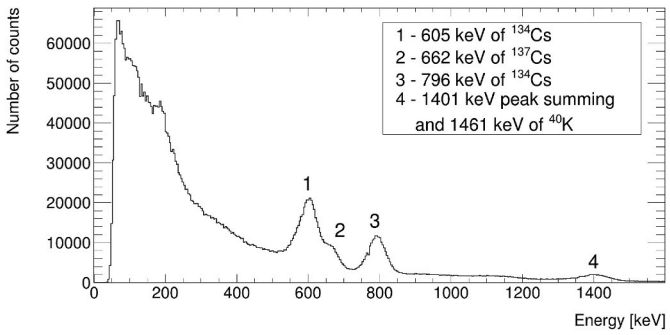

Fig. 7. Global gamma spectrum of ^{137}Cs and ^{134}Cs (samples shown in Fig. 6).

to coincide with an electron. Fig. 8 illustrates the outcome of implementing β/γ coincidence gating.

Compared to the total gamma spectrum (Fig. 7), the coincidence spectrum displays fewer counts at lower energies and a diminished background noise. The key observation is that the two peaks associated with ^{134}Cs stand out more clearly, and that the 662 keV ^{137}Cs peak does not appear anymore since this gamma is not emitted in time-coincidence (Fig. 5). One can notice a peak at 80 keV which originates from the X-rays fluorescence of the lead shield. The peak at 200 keV corresponds to the gamma backscattering. A Compton edge is noticeable around 400 keV (Knoll). The presence of the first low energy peak is discussed in section 3.1.4.

3.1.3. *Total autoradiographic image*

In order to get the final image, given each event, the values of x_β and y_β alone are then extracted, as presented in Fig. 3. By plotting these values, the radioactive map of Fig. 9 is obtained.

The image, with a count range set between 2 and 1000, clearly displays the distinct spatial distribution of radioactive events with minimal background interference.

3.1.4. *Autoradiographic image with γ time-coincidence*

By correlating the (x_β, y_β, E_γ) data, events with a non-zero E_γ were isolated in order to create the (x_β, y_β) radioactive distribution map (see Fig. 10).

The proportion of events framed by the red square in Fig. 10 represents 6.4 % of the original image population (see same region in Fig. 9). The resulting spectrum (in red in Fig. 10), associated with the region of interest of the ^{137}Cs sample, clearly brings out a low-energy peak.

In this region, the energy peak mean is around 35 keV, thus referring to the X-rays of the ^{137}Cs, as pinpointed by the decay scheme of Fig. 5. This energy region could lead to an incorrect identification of ^{134}Cs. Above this peak, on the [75; 1500] keV energy range, a very low number of coincidental γ rays of ^{137}Cs are populating the spectrum (1.1 % of the time coincidence gamma spectrum of Fig. 8), enhancing the ^{137}Cs rejection efficiency by β/γ coincidence in a specific energy range.

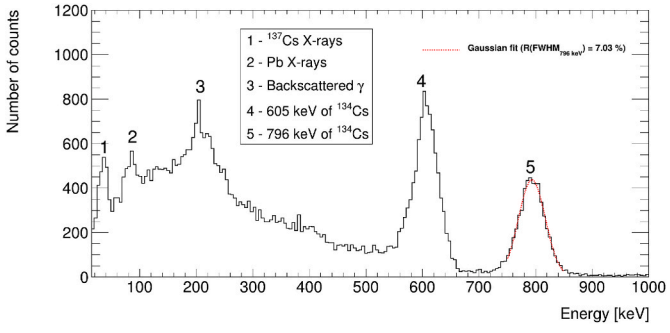

Fig. 8. Time-coincidence gamma spectrum of ^{137}Cs and ^{134}Cs.

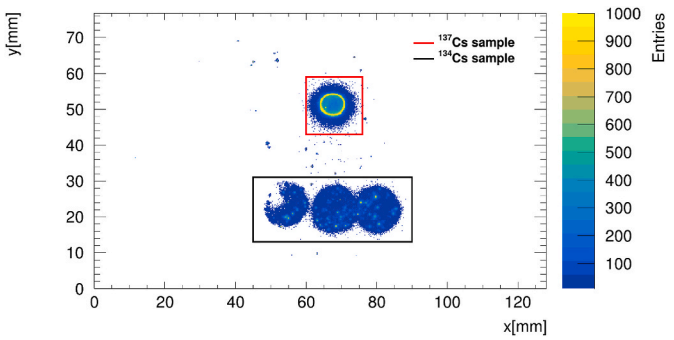

Fig. 9. Output of the position reconstruction method without gamma coincidence: Image of ^{134}Cs and ^{137}Cs (pixel size: 200 μm, z color scale is set to [2; 1000]). (For interpretation of the references to color in this figure legend, the reader is referred to the Web version of this article.)

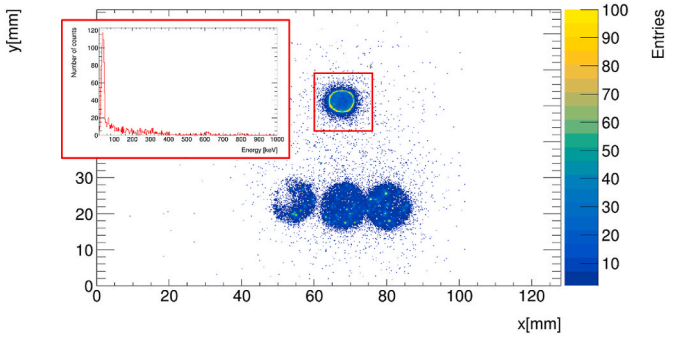

Fig. 10. Autoradiographic image with time-coincidence of ^{137}Cs and ^{134}Cs, and energy spectrum corresponding to the ^{137}Cs source region (pixel size: 200 μm).

3.1.5. *Autoradiographic image with β/γ time coincidence and energy range selection*

To further refine isotope discrimination, the gamma spectrum was restricted to the range from 100 keV to 900 keV. This energy window ensures that the misleading low-energy components (^{137}Cs X-rays) are excluded, while accommodating the highest gamma energy (796 keV) of the ^{134}Cs decay scheme. Fig. 11 displays the autoradiographic image obtained under these conditions. The fraction of events attributed to ^{137}Cs (red box) is then reduced to approximately 0.07 % through the combined effect of time coincidence and energy gating while keeping 6.8 % of the ^{134}Cs contoured in black in Fig. 9.

3.2. *Measurements of ^{134}Cs/^{137}Cs ratio with the β/γ coincidence system*

The separation algorithm was applied to samples with five known

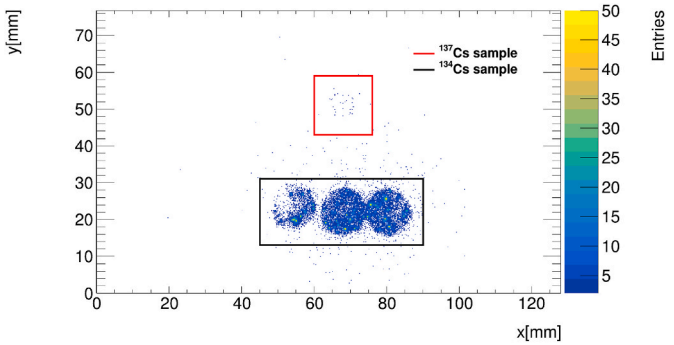

Fig. 11. Image of ^{134}Cs and ^{137}Cs with time coincidence events correlated to the [100; 900] keV energy range (pixel size: 200 μm).

activity ratios, labeled A_{Ri} (see Table 1). For each sample i, a count N_{0i} was recorded over the whole energy range and before any time coincidence rejection. An energy window W_j was then applied as well as the time coincidence algorithm and the corresponding count $N1_i$ was obtained contouring the deposited samples to identify ^{134}Cs population events. The ratio $R_i = \frac{N_{1i}}{N_{0i}}$ was plotted as a function of the activity ratio A_{Ri} and illustrated in Fig. 12. The length of associated error bars equals σ_{R_i} on either side of each point, with $\sigma_{R_i} = R_i\sqrt{\left(\frac{1}{N_{1i}} + \frac{1}{N_{0i}}\right)}$.

Three different energy windows were investigated to optimize the method.

- W_1 = [80 keV, 900 keV] includes nearly the entire gamma spectrum while excluding the low energy ^{137}Cs X-ray peak;
- W_2 = [540 keV, 900 keV] truncates the spectrum just before the first ^{134}Cs gamma peak;
- W_3 = [700 keV, 900 keV] isolates the prominent 795 keV gamma line of ^{134}Cs.

On Fig. 12, round markers are associated to the W_1 energy window, square markers to the W_2 one and triangle markers to the W_3 one. These different energy windows were selected to assess their impact on the linearity of the R versus A_R relationship. All three configurations yield linear fits with low χ^2 values, indicating that the method correlates the measured count ratio with the known activity ratio giving linear fit close to the range defined by error bars. One can notice that the χ^2 value is reduced when focusing on the highest energy peak in accordance with the spectrum of Fig. 10 in which the population of coincidental events above 700 keV is minimized. The choice of window allows optimization between maximizing count statistics and minimizing interference from overlapping peaks, thus confirming the efficiency and accuracy of the separation technique. However, it is important to note that sufficient calibration standards of known isotopic ratios must be prepared to obtain a standard curve (similar to Fig. 12) for such quantifications. These standards should also match the sample geometry and matrix closely. The reason is that the sample geometry and material would affect the detector efficiency and true coincidence summing correction of the gamma peaks.

3.3. Discussions

Future studies can also explore the use of the β/γ time coincidence to study the isotopic ratio of ^{135}Cs/^{137}Cs instead. Due to relatively shorter half-life of ^{134}Cs (2.07 years), ^{134}Cs/^{137}Cs isotopic ratio measurements could be limited by the detection limit after significant ^{134}Cs decay, years from the nuclear fallout or accident (Kubota et al. Takahashi, 2016). ^{135}Cs (half-life = 2.3×10^6 years) is a pure β-emitter, thus posing a challenge in conventional methods of measuring isotopic ratio with gamma spectroscopy. Typically, mass spectrometry must be used to obtain ^{135}Cs/^{137}Cs ratios (Snyder et al., 2012). Focusing on the ^{137}Cs X-rays, the β/γ coincidence device could be applied to tag ^{137}Cs emissions and to estimate the complementary ^{135}Cs contribution.

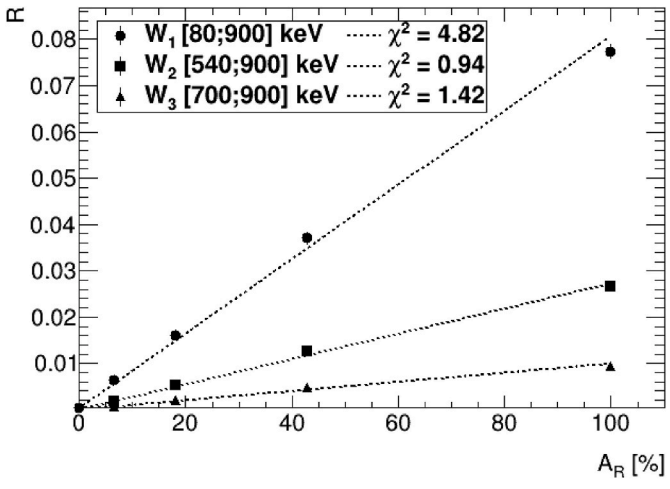

Fig. 12. Correlation between identified ^{134}Cs events among total counting (R) and ^{134}Cs activity proportion (A_R) for three energy range selections (W_j with j = 1, 2 or 3). Error bars are present but smaller than the marker size due to the high statistics of the measurement.

In the application of a nuclear accident response scenario such as the Fukushima Daiichi nuclear power plant accident, the ability to discriminate β-emissions from several radionuclides can be useful. For example, cesium-rich microparticles contain radionuclides such as technetium-99 (Ochiai et al., 2018). Developing a method to discriminate ^{99}Tc from Cs isotopes could facilitate radioactive particle isolation from a soil sample contaminated with high Cs activities.

This method takes advantage of counting-mode imaging, each reconstructed event corresponds to a unique disintegration, aiming to identify time coincidence between β emitted particles and γ photons. In the depicted system the detector dead time is 50 μs, the signal integration time and the chosen time coincidence gate width is 1.2 μs. One can notice that this method would not fit an integration-mode detector because pairing between the charge particle and the photon may not be performed.

The sensitivity of the prototype used in this study is quite low, mainly because of the photon detector acceptance. The small coverage surface $2\pi r$ and the long distance to the sample R lower the proportion of photons entering the photon detector entrance window (see Fig. 2). Indeed, according to Glen F. Knoll (Knoll), in the approximate of a point-like source, the geometric acceptance A, given by the formula: $A = \frac{1}{2}\left(1 - \frac{R}{\sqrt{R^2+r^2}}\right)$, equals 7.6 %.

In order to improve the coincidence setup sensitivity, one could imagine using a photon detector covering a larger solid angle with a higher yield and denser scintillating material (LYSO:Ce as an example) closer to the sample at the back of the petrographic glass slide inside the gas detector chamber thus limiting the attenuation of low-energy photons (mostly X-rays).

Another identified limiting factor of the detailed setup concerns the energy resolution. In more complex materials containing a large quantity of radioactive elements emitting γ photons with energy lines very close to each other, a better energy resolved photon detector would be necessary to precisely and wisely select energy gates. Nowadays, commercial CZT or HPGe based detectors can reach better than 2 % (FWHM) energy resolution (Mukhopadhyay et al., 2021).

4. Conclusions

We developed an autoradiographic spectroscopic method based on β/γ time coincidence applied to the ^{137}Cs and ^{134}Cs discrimination. The setup used in this study allows for an efficient rejection of radioactive decay events originating from the ^{137}Cs isotope in images containing both ^{134}Cs and ^{137}Cs cesium radioisotopes close to 100 %. With this new development, the isotopic radio of ^{134}Cs/^{137}Cs could allow for easier identification of the origin of the contamination by comparing with the calculated source term following a nuclear accident.

This hybrid charged particle/photon time coincidence energy gated imaging opens up new perspectives in autoradiographic based analysis in environmental sciences but also for biological preclinical studies. In the field of theranostics, this approach could be used to track either one isotope of a pair by selecting specific gamma emissions (annihilation gamma-rays from ^{64}Cu in the ^{64}Cu/^{67}Cu pair for example) in order to study competition or site saturation between imaging and therapeutic

vectors. In the context of targeted alpha therapy, this method could be of interest to follow the biodistribution of ^{225}Ac chain daughters like ^{221}Fr and ^{213}Bi which are known to be released from chelates by nuclear recoil and contribute to a dose release to healthy tissues.

CRediT authorship contribution statement

S. Duval: Writing – review & editing, Writing – original draft, Validation, Supervision, Resources, Conceptualization. **M. Libes De Geyter:** Writing – original draft, Data curation. **A. Bongrand:** Writing – review & editing, Investigation, Conceptualization. **E. Morteau:** Writing – review & editing, Resources, Investigation. **M. Siitari-Kauppi:** Writing – review & editing. **J.W.L. Ang:** Writing – review & editing, Resources, Investigation.

Declaration of competing interest

The authors declare the following financial interests/personal relationships which may be considered as potential competing interests: Samuel Duval reports a relationship with AI4R S.A.S. that includes: employment. He is a shareholder in AI4R, which manufactures the device "BeaQuant-S″ mentioned in this article. Eric Morteau reports a relationship with AI4R. He is a shareholder and consultant in AI4R S.A. S. Matias Libes De Geyter was employed during his internship at the AI4R S.A.S. company. Other authors declare that they have no known competing financial interests or personal relationships that could have appeared to influence the work reported in this paper.

Data availability

Data will be made available on request.

References

Adler, S.S., et al., 2025. A Quantitative Particle Identification (QPID) spectral autoradiography system. Commun. Eng. 4 (1), 1–11. https://doi.org/10.1038/s44172-025-00426-1.

Ang, J.W.L., et al., 2023. Improved radio-cesium detection using quantitative real-time autoradiography. ACS Omega 8 (25), 22523–22535. https://doi.org/10.1021/acsomega.3c00728.

Ang, J.W.L., et al., 2024. Detecting radioactive particles in complex environmental samples using real-time autoradiography. Sci. Rep. 14 (1), 5413. https://doi.org/10.1038/s41598-024-52876-w.

Bäck, T., Jacobsson, L., 2010. The alpha-camera: a quantitative digital autoradiography technique using a charge-coupled device for ex vivo high-resolution bioimaging of alpha-particles. J. Nucl. Med. Off. Publ. Soc. Nucl. Med. 51 (10), 1616–1623. https://doi.org/10.2967/jnumed.110.077578.

Barthe, N., Chatti, K., Coulon, P., Maîtrejean, S., Basse-Cathalinat, B., 2004. Recent technologic developments on high-resolution beta imaging systems for quantitative autoradiography and double labeling applications. Nucl. Instrum. Methods Phys. Res. Sect. Accel. Spectrometers Detect. Assoc. Equip. 527 (1), 41–45. https://doi.org/10.1016/j.nima.2004.03.014.

Billon, S., et al., 2020. Quantitative imaging of 226Ra ultratrace distribution using digital autoradiography: case of doped celestines. J. Environ. Radioact. 217, 106211. https://doi.org/10.1016/j.jenvrad.2020.106211.

Chino, M., et al., 2016. Utilization of 134Cs/137Cs in the environment to identify the reactor units that caused atmospheric releases during the Fukushima Daiichi accident. Sci. Rep. 6 (1), 31376. https://doi.org/10.1038/srep31376.

Donnard, J., Thers, D., Servagent, N., Luquin, L., 2009. High spatial resolution in β-Imaging with a PIM device. IEEE Trans. Nucl. Sci. 56 (1), 197–200. https://doi.org/10.1109/TNS.2008.2005673.

Donnard, J., Sardini, P., Descostes, M., 2025. Characterisation of radioactive decay series by digital autoradiography, part 2: experimental evidence of time and space coincidences (TSCs) on geo-materials. Nucl. Instrum. Methods Phys. Res. Sect. Accel. Spectrometers Detect. Assoc. Equip. 1075, 170439. https://doi.org/10.1016/j.nima.2025.170439.

Fabritius, O., et al., 2024. Radium sorption on crystalline rock; spatial distribution and sorption modeling study. Appl. Geochem. 162, 105930. https://doi.org/10.1016/j.apgeochem.2024.105930.

Ikehara, R., et al., 2020. Abundance and distribution of radioactive cesium-rich microparticles released from the Fukushima Daiichi nuclear Power plant into the environment. Chemosphere 241, 125019. https://doi.org/10.1016/j.chemosphere.2019.125019.

G. F. Knoll, Radiation Detection and Measurement, fourth ed. John Wiley & Sons, Inc.

Kubota, T., et al., 2016. Isotopic ratio of 135Cs/137Cs in Fukushima environmental samples collected in 2011. In: Takahashi, T. (Ed.), Radiological Issues for Fukushima's Revitalized Future. Springer Japan, Tokyo, pp. 25–31. https://doi.org/10.1007/978-4-431-55848-4_3.

Lefeuvre, H., Billon, S., Descostes, M., Donnard, J., Duval, S., Sardini, P., 2024. Using spectroscopic autoradiography of alpha particles for the quantitative mapping of 226Ra ultra-traces in geo-materials. J. Environ. Radioact. 273, 107392. https://doi.org/10.1016/j.jenvrad.2024.107392.

Leskinen, A., Fichet, P., Siitari-Kauppi, M., Goutelard, F., 2013. Digital autoradiography (DA) in quantification of trace level beta emitters on concrete. J. Radioanal. Nucl. Chem. 298 (1), 153–161. https://doi.org/10.1007/s10967-013-2535-6.

Miller, B.W., Gregory, S.J., Fuller, E.S., Barrett, H.H., Barber, H.B., Furenlid, L.R., 2014. The iQID camera: an ionizing-radiation quantum imaging detector. Nucl. Instrum. Methods Phys. Res. Sect. Accel. Spectrometers Detect. Assoc. Equip. 767, 146–152. https://doi.org/10.1016/j.nima.2014.05.070.

Mukhopadhyay, S., Maurer, R.J., Biery, M.B., Guss, P.P., 2021. Evaluation and benchmarking of a commercial Cadmium Zinc Telluride (CZT) gamma imaging camera. Nevada National Security Site/Mission Support and Test Services LLC (NNSS/MSTS), North Las Vegas, NV (United States). https://doi.org/10.2172/1808845. DOE/NV/03624-1134.

Muuri, E., et al., 2019. Electronic autoradiography of 133Ba particle emissions; diffusion profiles in granitic rocks. Appl. Radiat. Isot. 149, 108–113. https://doi.org/10.1016/j.apradiso.2019.04.026.

Ochiai, A., et al., 2018. Uranium dioxides and debris fragments released to the environment with cesium-rich microparticles from the Fukushima daiichi nuclear power plant. Environ. Sci. Technol. 52 (5), 2586–2594. https://doi.org/10.1021/acs.est.7b06309.

Sardini, P., Donnard, J., Descostes, M., 2024. Characterisation of radioactive decay series by digital autoradiography, part 1: a theoretical approach using time and space coincidence (TSC) analysis. Nucl. Instrum. Methods Phys. Res. Sect. Accel. Spectrometers Detect. Assoc. Equip. 1069, 169832. https://doi.org/10.1016/j.nima.2024.169832.

Snyder, D.C., Delmore, J.E., Tranter, T., Mann, N.R., Abbott, M.L., Olson, J.E., 2012. Radioactive cesium isotope ratios as a tool for determining dispersal and re-dispersal mechanisms downwind from the Nevada nuclear security site. J. Environ. Radioact. 110, 46–52. https://doi.org/10.1016/j.jenvrad.2012.01.019.

Soti, Z., Magill, J., Dreher, R., 2019. Karlsruhe Nuclide Chart - New 10, edition 2018, 5. https://doi.org/10.1051/epjn/2019004. 6–6.

Wai, K.-M., Krstic, D., Nikezic, D., Lin, T.-H., Yu, P.K.N., 2020. External Cesium-137 doses to humans from soil influenced by the Fukushima and chernobyl nuclear power plants accidents: a comparative study. Sci. Rep. 10 (1), 7902. https://doi.org/10.1038/s41598-020-64812-9.

Yamamoto, S., et al., 2025. High resolution and energy resolved imaging of astatine-211 administered sliced mouse using a 1 mm size Si-PM based GGAG alpha particle imaging detector. Radiat. Phys. Chem. 232, 112605. https://doi.org/10.1016/j.radphyschem.2025.112605.

Livechart - Table of nuclides - nuclear structure and decay data [Online]. Available. https://www-nds.iaea.org/relnsd/vcharthtml/VChartHTML.html. (Accessed 22 April 2025).